Protection and Control of Modern Power Systems

ORIGINAL RESEARCH

Open Access

Solar-PV inverter for the overall stability of power systems with intelligent MPPT control of DC-link capacitor voltage

Sheetal Singh[1,2*], Sanju Saini[1], S. K. Gupta[1] and Rajeev Kumar[1,2*]

Abstract

This paper demonstrates the controlling abilities of a large PV-farm as a Solar-PV inverter for mitigating the chaotic electrical, electromechanical, and torsional oscillations including Subsynchronous resonance in a turbogenerator-based power system. The oscillations include deviations in the machine speed, rotor angle, voltage fluctuations (leading to voltage collapse), and torsional modes. During the night with no solar power generation, the PV-plant switches to PV-STATCOM mode and works as a Solar-PV inverter at its full capacity to attenuate the oscillations. During full sun in the daytime, on any fault detection, the PV-plant responds instantly and stops generating power to work as a Solar-PV inverter. The PV-farm operates in the same mode until the oscillations are fully alleviated. This paper manifests the control of the DC-link capacitor voltage of the Solar-PV inverter with a bacterial foraging optimization-based intelligent maximum power point tracking controller for the optimal control of active and reactive power. Kundur's multi-machine model aggregated with PV-plant is modeled in the Matlab/Simulink environment to examine the rotor swing deviations with associated shaft segments. The results for different test cases of interest demonstrate the positive outcomes of deploying large PV-farms as a smart PV-STATCOM for controlling power system oscillations.

Keywords PV-STATCOM, Power oscillations, Grid-connected system, BFO algorithm, Rotor dynamics

1 Introduction

The growing demand for clean energy has drawn attention to renewable energies like wind and solar. The use of renewable energy has many advantages. However, these renewable sources, when used at large scale, significantly alter power network stability in a number of ways. This leads to a shift in research focus to the alternatives to exploit the untapped capabilities of these RPPs (Renewable Power Plants) for power system stability enhancement. For example, wind is prominent amidst all renewable sources, and the active role of DFIG (doubly-fed induction generator) in alleviating power oscillations is now recognized and established [1, 2]. Solar-PV contributes a significant proportion considering the other renewable generating units of current interest, and Solar-PV farms are the fastest-growing industry in the renewable sector and are rapidly increasing their proportion. Because of the extensive installation of WPPs (Wind Power Plants), the overall competency of these large scale PV-farms has grown [3–5], though the present PV penetration level is marginal concerning the optimal demand. This needs to be augmented by establishing more PV-farms across the globe. The overall growth rate indicates that it will touch 10–15% within a decade [6], and several large scale PV-plants of more than 100 MW are in operation while many more even larger ones are planned [7–10]. With the growing penetration of PV generating units

*Correspondence:
Sheetal Singh
sheetal08041988@gmail.com; sheetalsingh@kiet.edu
Rajeev Kumar
rajeev.rakshit@gmail.com; rajeev.kumar@kiet.edu
[1] Electrical Engineering Department, Deenbandhu Chhotu Ram University of Science and Technology Murthal, Murthal, India
[2] Electrical and Electronics Engineering Department, KIET Group of Institutions, Ghaziabad, India

the prime concern is to examine their effectiveness in the suppression and control of power oscillations by using and controlling inverter capabilities. In [11–14], power system oscillations are damped with PV-plants, whereas a unique idea of using large-scale PV plants as STATCOM was first introduced and commissioned in 2009 [15, 16]. The concept, termed PV-STATCOM, proposes the use of the overall inverter capability of PV-farms when sunlight is not available for solar power generation and hence operating in full STATCOM mode during night-time. In addition, the remaining inverter capability after the solar power generation in the daytime was used for different ancillary supports like voltage regulation [15], growing the connectivity among the Solar-PV farms, and enhancing the power transfer capability of the transmission lines [17, 18]. A major drawback of this concept is that the Solar-PV inverters cannot be used when solar power generation is in full swing. A novel technology [19] is exploited in [20] to build a Solar-PV inverter, where the inverter abilities of a Solar-PV farm are fully used both after sunset and during the sunlight in day time at any stage when required for alleviating SSR (Subsynchronous resonance) [21–24].

1.1 Recent advances

In [25], large-scale PV-farms were deployed for SSR control and alleviation. In [20], the Solar-PV inverter was used as STATCOM [26] for mitigation and control of SSR oscillations for power system stability. In [27], the power system oscillations were stabilized using a synchronous MG (motor-generator) pair. Power oscillation dampings with PV-STATCOM were presented in [28], and [29] controlled the power system voltage using a smart Solar-PV inverter. In [30], an adaptive compensation scheme alleviated the power oscillations by controlling large PV-farms, while alleviation of electromechanical oscillations using a PV-farm was presented in [31]. Reference [32] proposed a unique control scheme to use the utility-scale PV-plants to mitigate power oscillations for stability enhancement. In [33], a novel controller was designed and deployed for the stability of a grid-integrated PV-plant, whereas [34] aided inertia using a virtual alternator to control the frequency of a PV-integrated power system. Reference [35] proposed synchro power controllers to stabilize the system with rising PV penetration, while voltage support of power systems using grid-tied PV-farms has been discussed in [36]. In [37], an intelligent PV system enhanced the electrical modes of the power system in a smart grid, and in [38], power system frequency was controlled and stabilized by manipulating the lagging VAR supplied by PV-STATCOM. Reference [39] controlled a largescale PV plant as a Solar-PV inverter to alleviate the oscillations and support frequency regulation to stabilize the power system. In [40], post-fault voltage recovery was supported with a Solar-PV inverter to aid system stability.

1.2 Impact of soft computing techniques in the domain

Soft computing-based metaheuristic optimizers are now highly popular for deriving optimal control parameters and solving problems in daily life to the complex mathematical domain. In [25], a human-based metaheuristic optimizer was used to dampen low-frequency power oscillations using a large-scale PV-farm. Reference [41] exploited the swarm abilities of another metaheuristic optimizer for optimally regulating the control signals to stabilize the power system. In [42], SSR was damped and alleviated with a PSO optimizer and in [43], the output power of a hybrid Wind-PV farm was controlled using a hybrid metaheuristic optimization technique in response to the system oscillations to produce the stabilizing effect. Another swarm-based algorithm WOA (Whale optimization algorithm) was proposed in [44] for optimally controlling a Type-2 WPP to mitigate low-frequency oscillations. In [45], IG-based WPP oscillations were controlled with BFO-based LQR. In [46], another metaheuristic hybrid algorithm was used to control the frequency of a PV-coupled three-area power system. Power system stability improvement with intelligent PSS control was demonstrated in [47].

With the growing trend of modern metaheuristic algorithms and rising PV penetration, this paper examines the ability of the BFO optimizer in optimizing the inverter capabilities of a grid-connected solar farm for quenching and controlling the chaotic oscillations in a series-compensated [44] multi-machine system.

This paper explicitly demonstrates the merits of a PV-plant as a Solar-PV inverter for quenching and suppressing the different oscillatory modes, including rotor fluctuations, coupling voltage, and shaft torsional movements causing SSR for both steady and transient states. The basic controller of the Solar-PV inverter is the same as that in [20]. With the advantages of soft computing-based intelligent techniques SPS:refid::bib41|bib42|bib43|bib44|bib45|bib46|bib47[41–47], this paper proposes BFO [48, 49] for optimal control to achieve the desired outcomes in terms of the least settling time and more negative eigenvalues for different system modes of interest. A comprehensive tabular analysis of the present work compared with previous studies is presented in Table 1.

The paper presents the following points which, to the author's best knowledge, have not been considered in earlier studies:

- A Solar-PV inverter is made to operate as a PV-STATCOM to stabilize the different modes of a Turbogenerator-based power system.

Table 1 This work versus previous studies (a comparative analysis)

Previous works	Inverting technique	Control technique	Attribute
[20]	Solar-PV Inverter	Traditional	Electrical + Torsional mode
[25]	Solar-PV Inverter	Intelligent (Metaheuristic; Human Based)	Electrical + Torsional mode
[28]	Solar-PV Inverter	Traditional	Electrical mode
[29]	Solar-PV Inverter	Smart	Electrical + Electromechanical mode
[30]	Solar-PV Inverter	Intelligent; (ANFIS)	Electrical + Electromechanical mode
[31]	Solar-PV Inverter	Traditional	Electromechanical mode
[32]	Solar-PV Inverter	Traditional	Electrical + Electromechanical mode
[36]	Solar-PV Inverter	Traditional	Electrical + Electromechanical mode
[37]	Solar-PV Inverter	Smart	Electrical + Electromechanical mode
[39]	Solar-PV Inverter	Traditional	Electrical + Electromechanical mode
[56]	Solar-PV Inverter	Intelligent (Metaheuristic; Swarm-Based)	Electrical mode
This work	Solar-PV Inverter	Intelligent (Metaheuristic; Swarm-Based)	Electrical + Electro-mechanical + Torsional mode

- An intelligent MPPT control of the DC-Link capacitor voltage is implemented and introduced for optimal control.
- It is the first time that an intelligent controller is optimally controling the inverter side voltage of a large-scale PV farm.
- A swarm-based optimizer tunes the outputs of the Solar-PV inverter for overall stability and control using the classical PWM (Pulse width modulation) approach.

The remainder of the paper is organized as follows: Section II presents the PV modelling and Section III describes the multi-machine system comprising four conventional turbogenerators. Section IV presents the suggested BFO-based inverter control scheme, while Section V presents a detailed analytical discussion with supporting graphics. Finally, Section VI summarizes and concludes the paper.

2 Solar-PV inverter

This paper considers a standard model of a PV-farm. This has already been used and validated for power system stability analysis in many studies [14, 25].

Even though the PV generators [14] are dispersed throughout the solar farm, as is the case in wind farms, the aggregate PV power is transmitted using a single integrated unit. Consequently, all the Solar-PV units inside the farm are integrated to operate as a single generator with equivalent MVA equalling the aggregated rating of all PV-generators. Since the converter-coupled PV-generators are capable of also exchanging lagging VAR, the large-scale PV-plant can be simulated as an alternator, i.e., the large-scale solar farm may be assumed to be a load or generator bus of proper limit [12], as is the case in several studies [11–14, 28], In this paper, the PV-farm is simulated as a unit generator capable of delivering real and reactive powers.

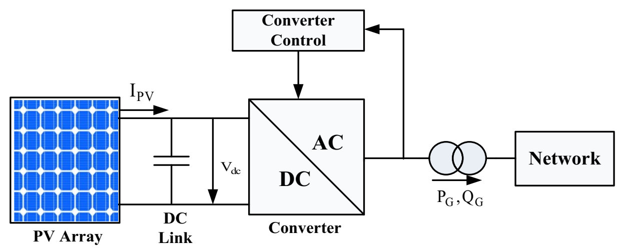

Fig. 1 A single unit PV generator with the control unit

The basic unit of a Solar-PV farm is a PV generator. A PV-generating unit, as shown in Fig. 1, comprises mainly three elements: (1) PV-array; (2) converter; and (3) controller.

The overall equation of the output current for the array is represented as [14]:

$$I_{PV} = I_{SCA}(G) - N_P * I_O\left[EXP\frac{(V_A + I_{PV}R_S)q}{nN_s kT} - 1\right] \tag{1}$$

A large scale PV-farm contains N PV units. The power system stability analysis incorporating the PV-farms is realized as a single generating unit model obtained by aggregating the N individual PV-generators. In this paper, the NREL (National Renewable Energy Laboratory) equivalence method is adopted to build the large PV-farm single-unit generator. The NREL aggregating method from the single generator equivalent model is:

$$Z_{eq} = \frac{\sum_{i=1}^{l} Z_i n_i^2}{N^2} \tag{2}$$

$$B_{eq} = \sum_{i=1}^{l} B_i \tag{3}$$

The entire study is carried out with a 300 MVA single generator equivalent PV-farm [20], built of 300 individual PV-generators of 1 MVA each [14].

3 The multimachine system

The Solar-PV operation modes have already been discussed and described in [20]. In this paper, Kundur's multi-machine model [22], integrated with a PV-farm, is realized and modeled in Matlab software to examine system stability, including the torsional modes (SSR).

As shown in Fig. 2a, the generator 1 of area 1 is modeled as the IEEE FBM comprising several segments with considerable inertia viz the different turbine units: HP, IP, low-pressure turbines (LP_A, LP_B), alternator, and exciter connected with different shaft segments. Zero damping is assumed to cast the worst conditions. The synchronous generator parameters, including the shaft segments, are the same as those in [50]. The alternator rated at 892.4 MVA is operating at 500 MW. A 300 MVA single generator equivalent PV-plant is associated with the PV bus enabling the aggregate power produced at the generating end to comply with [50]. The model parameters are identical to those of Kundur's two-area model [21], rationalized on 100 and 892.4 MVA bases. The line is compensated at its optimal level and is fixed at 80%. An aggregated large-scale PV-farm is associated with the voltage-controlled bus with a line of 25 km in length to exchange the active and reactive powers at the common bus following the machine's oscillatory movements. The PV-farm is realized using a static converter comprising a total of 6 IGBTs employing a static capacitor for the DC supply having volt-ampere characteristics the same as that of the solar panel in a largescale PV-farm [17, 51]. The PV-farm is made to operate at the optimal point during its normal operation with the MPPT technique [52, 53], and a static capacitor at the converter DC side holds the DC voltage at a fixed value [54]. An LLL-G fault is introduced between buses 8–9, while the chaos produced because of the perturbations, introduced like an LLG-fault, change in electric torque, etc., is stabilized using the proposed BFO-tuned PV-STATCOM.

3.1 The multi-machine modelling

The multi-machine sub-transient modeling has been presented in [55]. Post-fault analysis of alternators can be realized using the sub-transient model comprising four windings (viz. a field winding accompanied by an amortisseur coil at the d-axis, and two amortisseur windings at the q-axis) of the rotor.

For 'm' synchronous machines of P-poles let θ_{shaft} be the total angular displacement of the rotor's d-axis concerning the stator axis (α-axis). The rotor speed of the *i*th alternator in electrical rad/sec, is given as:

$$\omega_i = \frac{P}{2} \times \frac{d\theta_{shaft}}{dt} \tag{4}$$

The rotor angle δ is supposed to be constant for uniform shaft speed:

$$\delta = \frac{P}{2}.\theta_{shaft} - \omega_s t \tag{5}$$

Hence, for the ith machine, Eq. (5) is written as:

$$\frac{d\delta_i}{dt} = \omega_i - \omega_s \tag{6}$$

The dynamics of the *i*th generator are governed by the swing equation, as:

$$\frac{2H}{\omega_s}.\frac{d^2\delta}{dt^2} = T_{mi} - T_{ei} \tag{7}$$

Here, machine inertia is shown by H, T_e stands for electromechanical torque and T_m is the mechanical torque. Using the sub-transient model of the *i*th machine, Eq. (7) may be written as:

$$\begin{aligned}\frac{d\omega_i}{dt} =& \frac{\omega_s}{2H}\Bigg[T_{mi} - D(\omega_i - \omega_s) - \frac{\left(x''_{di} - x_{lsi}\right)}{\left(x'_{di} - x_{lsi}\right)}E'_{qi}I_{qi} \\ & - \frac{\left(x'_{di} - x''_{di}\right)}{\left(x'_{di} - x_{lsi}\right)}\psi_{1di}I_{qi} - \frac{\left(x_{qi} - x_{lsi}\right)}{\left(x'_{qi} - x_{lsi}\right)}E'_{di}I_{di} \\ & + \frac{\left(x'_{qi} - x_{qi}\right)}{\left(x'_{qi} - x_{lsi}\right)}\psi_{2qi}I_{di} + \left(X''_{di} - X''_{di}\right)I_{qi}I_{di}\Bigg]\end{aligned} \tag{8}$$

where the direct axis (d-axis) components for the *i*th machine are: I_{di}—Armature current (d-axis). X''_{di}—Sub-transient reactance (d-axis). X'_{di}—Transient reactance (d-axis). X_{di}—Synchronous reactance (d-axis). T'_{doi}, T''_{doi} —Transient and Sub-transient time constants (d-axis).

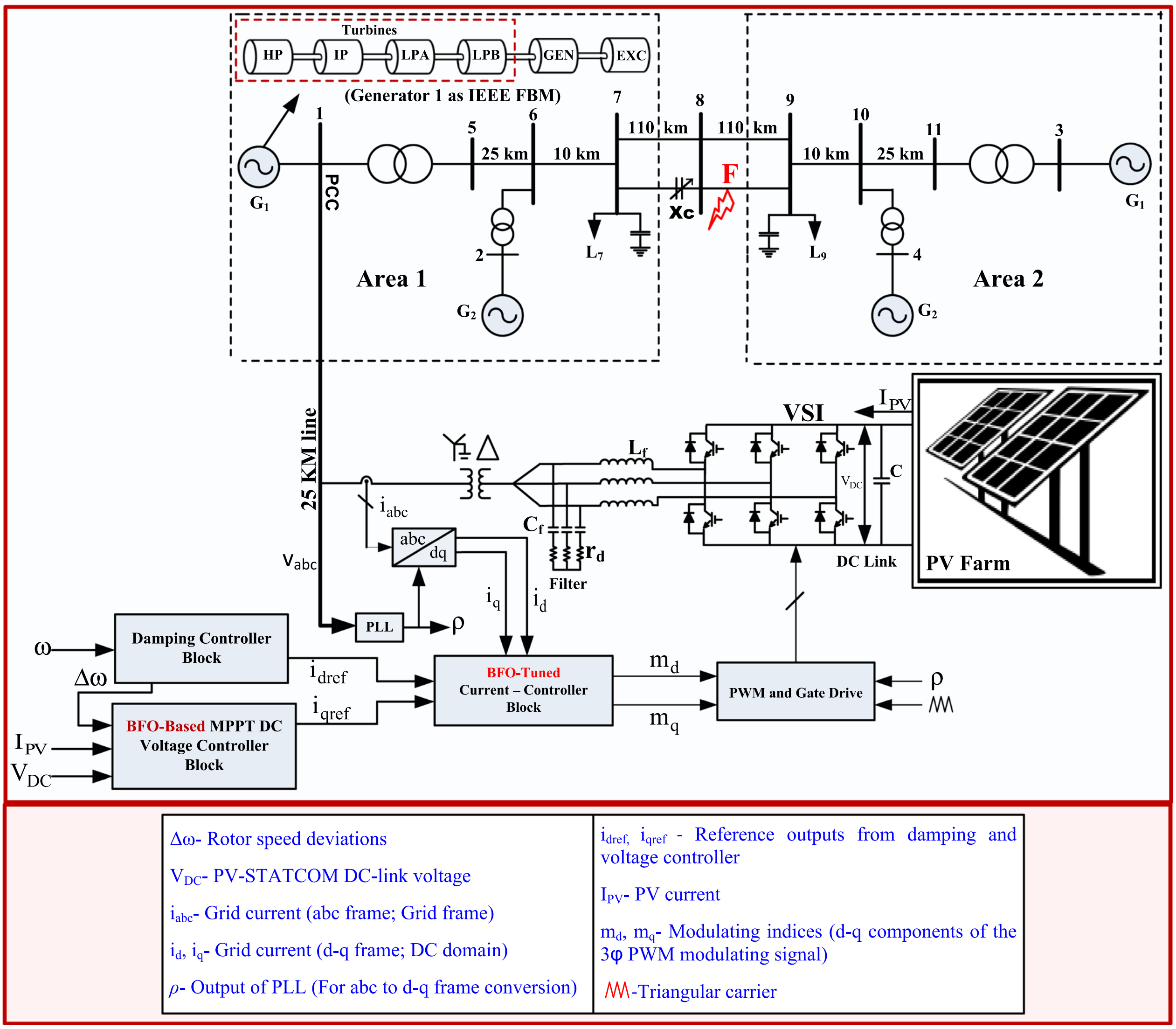

(a). Kundur's multi-machine model aggregated with PV-farm

Fig. 2 **a** Kundur's multi-machine model aggregated with PV-farm, **b** the proposed control topology

Similarly, I_{qi} is the quadrature axis component of the stator current, and X''_{qi}, X'_{qi} and X_{qi} are the q-axis components of the sub-transient, transient, and synchronous reactances, respectively. T''_{qoi} and T'_{qoi} are the q-axis sub-transient and transient time constants, respectively.

The transients in the emf because of field linkage (E'_{di}) and quadrature axis amortisseur windings $\left(E'_{qi}\right)$ are mathematically presented as:

$$\frac{dE_{qi'}}{dt} = \frac{1}{T_{doi'}}\left[-E'_{qi} - (X_{di} - X_{di'}\left\{-I_{di} - \frac{(x'_{di} - x''_{di})}{(x'_{di} - x_{lsi})^2}(\psi_{1di} - (X'_{di} - X_{lsi})I_{di} - E_{qi'})\right\} + E_{fdi}\right] \tag{9}$$

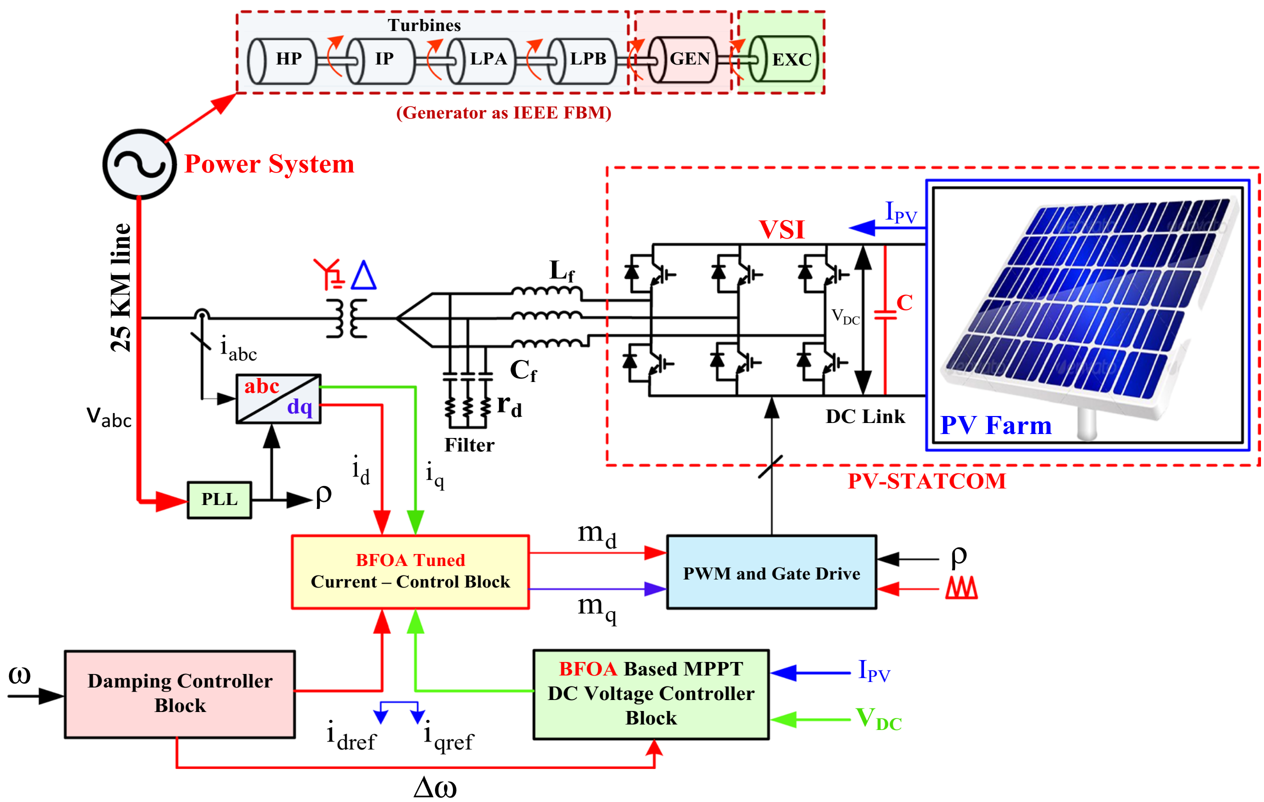

(b). The proposed control topology

Fig. 2 continued

$$\frac{dE_{di'}}{dt} = \frac{1}{T_{qoi'}}\left[-E'_{di} - (X''_{qi} - X_{qi'})\left\{I_{qi} - \frac{\left(x'_{qi} - x_{qi}\right)}{\left(x'_{qi} - x_{lsi}\right)^2}\left(-\psi_{2qi} + (X'_{Qi} - X_{lsi})I_{qi} - E_{di'}\right)\right\}\right] \tag{10}$$

ψ_{1di} and ψ_{2qi} represent the sub-transient emf that arise because of linking flux in the direct and quadrature axes amortisseur coils, and can be mathematically presented as:

$$\frac{d\psi_{1di}}{dt} = \frac{1}{T''_{doi}}\left[-\psi_{1di} + E'_{qi} + \left((X'_{di} - X_{lsi}\right)I_{di}\right] \tag{11}$$

$$\frac{d\psi_{2qi}}{dt} = \frac{1}{T''_{qo}}\left[\psi_{2qi} + E'_{di} - \left(X'_{qi} - X_{lsi}\right)I_{qi}\right] \tag{12}$$

$$V_i\cos\left(\delta_i - \theta_i\right) - \frac{\left(x''_{di} - x_{lsi}\right)}{\left(x'_{di} - x_{lsi}\right)}E'_{qi} - \frac{\left(x'_{di} - x''_{di}\right)}{\left(x'_{di} - x_{lsi}\right)}\psi_{1di} + R_{si}I_{qi} - X_{di}I_{di} = 0 \tag{13}$$

$$V_i sin(\delta_i - \theta_i) + \frac{\left(x''_{qi} - x_{lsi}\right)}{\left(x'_{qi} - x_{lsi}\right)}E'_{di} - \frac{\left(x'_{qi} - x''_{qi}\right)}{\left(x'_{qi} - x_{lsi}\right)}\psi_{2qi} - R_{si}I_{di} - X_{qi}I_{di} = 0 \tag{14}$$

Equations (4–12) present the machine rotor dynamics in differential equations. The armature quantities concerning stability analysis are supposed to be associated with the source terminal parameters and expressed as algebraic Eqs. (13, 14):where V_i: machine terminal voltage. R_{si} : armature resistance. X_{lsi}: armature leakage reactance.

3.2 Exciter modeling

The exciter comprises a separately excited DC generator and supplies excitation current to the field windings on the rotor. The saturation function in the IEEE DC1A exciter is mathematically expressed as:

$$S_E\left(E_{fd}\right) = A_s e^{BsE_{fd}} \tag{15}$$

where E_{fdi} stands for the excitation voltage of the ith machine. A_s and B_s are derived from the saturation curve. The exciter is modeled as:

$$\frac{dV_{tri}}{dt} = \frac{1}{T_{ri}}[-V_{tri} + V_{ti}] \tag{16}$$

$$\frac{dE_{fdi}}{dt} = -\frac{1}{T_{Ei}}\left[K_{Ei}E_{fdi} + E_{fdi}A_{ex}e^{B_{ex}E_{fdi}} - V_{ri}\right] \tag{17}$$

$$\frac{dV_{ri}}{dt} = \frac{1}{T_{Ai}}\left[\frac{K_{Ai}K_{fi}}{T_{Fi}}R_{Fi} + K_{Ai}\left(V_{refi} - V_{tri}\right) - \frac{K_{Ai}K_{fi}}{T_{Fi}}E_{fdi} - V_{ri}\right] \tag{18}$$

$$\frac{dR_{Fi}}{dt} = \frac{1}{T_{Fi}}\left[-R_{Fi} + E_{fdi}\right] \tag{19}$$

where V_{tri} and V_{ti} are the voltage state variable and terminal voltage, respectively.

3.3 PSS model

PSS is mathematically modeled and expressed with speed deviations as an input signal, as:

$$V_{pssi} = K_{pssi}\frac{sT_\omega}{(1 + sT_\omega)}\frac{(1 + sT_{1i})}{(1 + sT_{2i})}\frac{(1 + sT_{3i})}{(1 + sT_{4i})} \tag{20}$$

where T_w: Time constant of washout. K_{psssi}: PSS gain. T_{1i}, T_{2i},T_{3i}, T_{4i}: Time constants for the lead-lag compensator.

The constant T_w nullifies the steady-state error in the reference voltage because of the speed deviations. The lead-lag constant T_{1i}, T_{2i}, T_{3i}, and T_{4i} are tuned to dampen and suppress the oscillations over the frequency range over which the oscillations arise.

4 Inverter control scheme incorporating BFO algorithm

4.1 Inverter controller

The primary inverter controller of the proposed Solar-PV inverter resembles the state-of-the-art controller [20] and is shown in Fig. 2b.

The controller components are reproduced here for clarity only. The primitive controller mainly consists of three control blocks, viz. current, damping, and DC voltage control. The Solar-PV control block [20] uses the alternator speed deviations as a control signal for generating auxiliary stabilizing signals that develop the torque components against the sub-synchronous oscillations.

The generator speed deviations comprise all the oscillatory information related to electrical, electromechanical, and torsional modes that may exist in a turbine-coupled turbo alternator system. The Solar-PV inverter is assembled at the turbine-generator terminal and hence instantly senses any speed deviation in the turbogenerator. The inverter controller is designed to operate in the DC domain (*d-q* frame), so the controller voltage is held in synchronism with the power system PCC voltage using the PLL (Phase-locked loop). The PLL angle θ computes the *d-q* components of the 3-ϕ grid voltage and current (V_d, V_q, I_d, I_q). The current components I_d and I_q govern the active and reactive powers of the Solar-PV inverter.

4.1.1 Damping controller

The damping block shown in Fig. 3 instantly senses any speed deviations (Δω), with the help of the washout block. The deviation is further augmented with a gain K and reversed by a 180-degree phase shift to get the reference current I_{dref} which acts as an input to the current regulator. Thus, the damping controller generates the reference current I_{dref} for regulating the Solar-PV inverter reactive power in accordance with the turbogenerator oscillations.

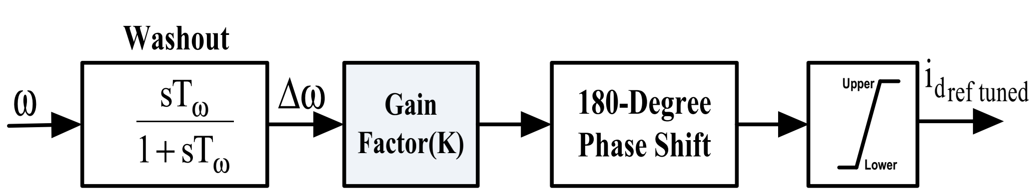

Fig. 3 Damping control block

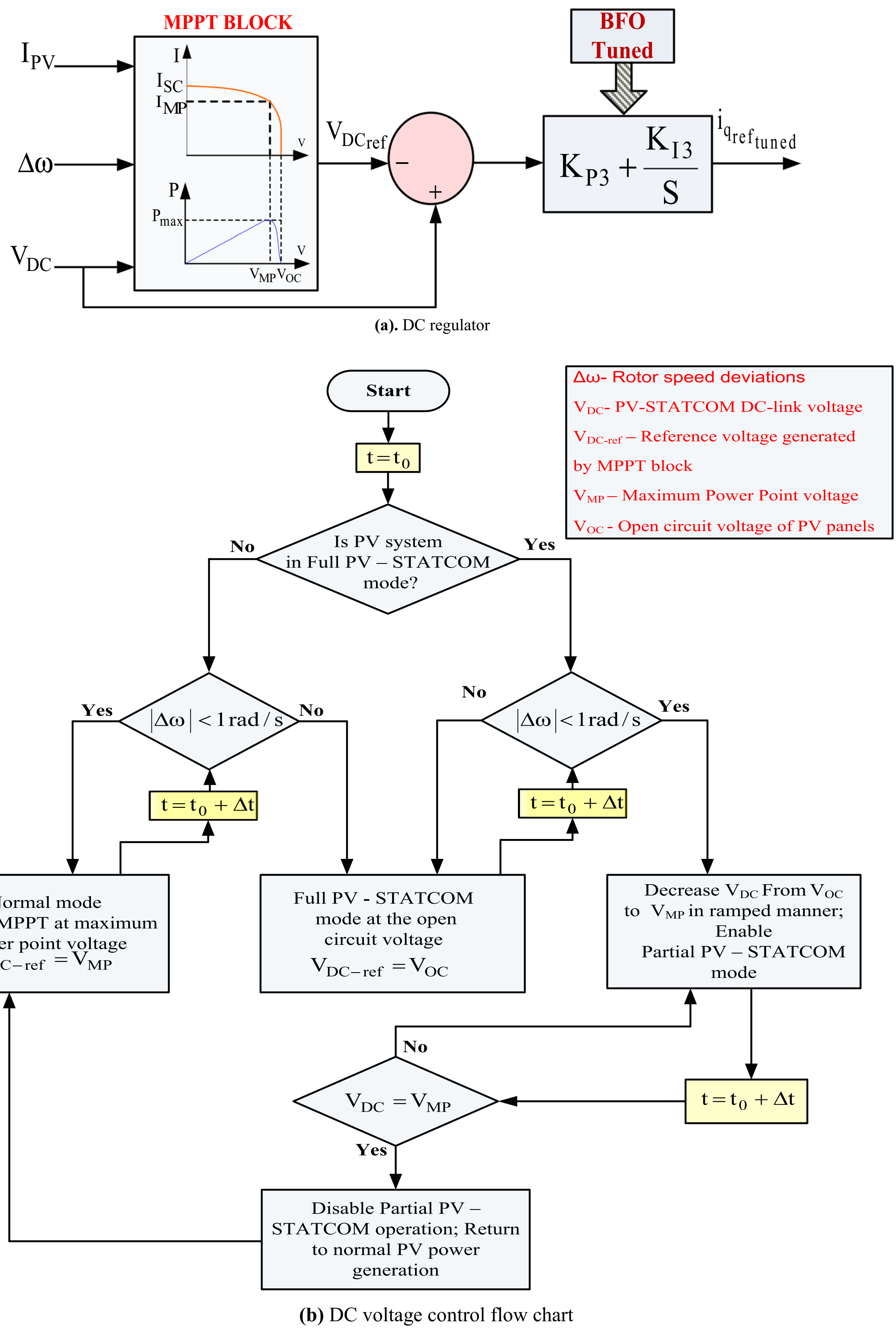

Fig. 4 **a** DC regulator, **b** DC voltage control flow chart

4.1.2 DC voltage regulator

The DC voltage controller depicted in Fig. 4a includes MPPT as a subsystem to maintain the inverter-side DC voltage V_{DC} of the Solar-PV inverter. With the input of converter side voltage (V_{DC}) and solar-current (I_{PV}), the MPPT generates a reference voltage V_{DCref} for controlling the actual power of the PV-farm. The error produced on comparing the converter side voltage (V_{DC}) and reference voltage V_{DCref} is processed with the PI controller and a reference current I_{qref} is generated and fed to the current regulator. The BFO optimizer monitors and optimally tunes the controller gain.

The flowchart presented in Fig. 4b portrays the overall working of the intelligent MPPT-based DC regulator. The DC voltage regulator continuously observes the system conditions to check whether the system is working satisfactorily, i.e., if the system parameters are under predefined values (if Δω < 1 rad/s). At this stage, the solar farm continues generating the normal power at its full capacity and $V_{DCref} = V_{MP}$. Once a disturbance is observed above the threshold value (e.g., Δω > 1 rad/s), the PV-plant stops the power generation instantly and the Solar-PV inverter is immediately switched to full STATCOM mode with V_{DCref} set to V_{OC}. Once the system is stabilized, e.g., when Δω < 1 rad/s, the Solar-PV inverter steadily returns to active power production by reducing V_{DC} to the prefault value V_{MP}. At this stage, the Solar-PV inverter starts operating in partial PV-STATCOM mode, i.e., when the Solar-PV inverter is resuming active power production, the PV-inverter still operates as PV-STATCOM for mitigating the disturbances with remaining capacity left after the real power production until $V_{DC=V_{MP}}$. The partial PV-STATCOM mode is then fully disabled and PV power generation is completely restored to the initial prefault level without any interruption in the disturbance alleviation process.

4.1.3 The current regulator

The current regulator in Fig. 5 is part of the inner-loop and controls the Solar-PV inverter voltage in response to the rotor speed deviation. First, the *d-q* components (I_d and I_q) of the grid 3-ϕ current is compared to the reference currents (I_{dref} and I_{qref}). The error produced is then fed to the current regulator (PI controller), the output of which is further processed and magnified with the decoupled feed-forward loop. The augmented signal is then normalized to derive the d-q component (m_d, m_q) of the 3-ϕ PWM modulating signal (m_{abc}), which is further compared to a carrier wave of high frequency to synthesize the IGBT switching signals. The switching ripples on the inverter AC-side are attenuated using LCL filters.

The role of BFO-based PI controller The PI controller makes the current regulator generate the required converter output voltage. This is fed to the PWM modulator to produce the gate signals, until the d-axis grid current I_d matches the desired I_{dref} generated by the damping controller block

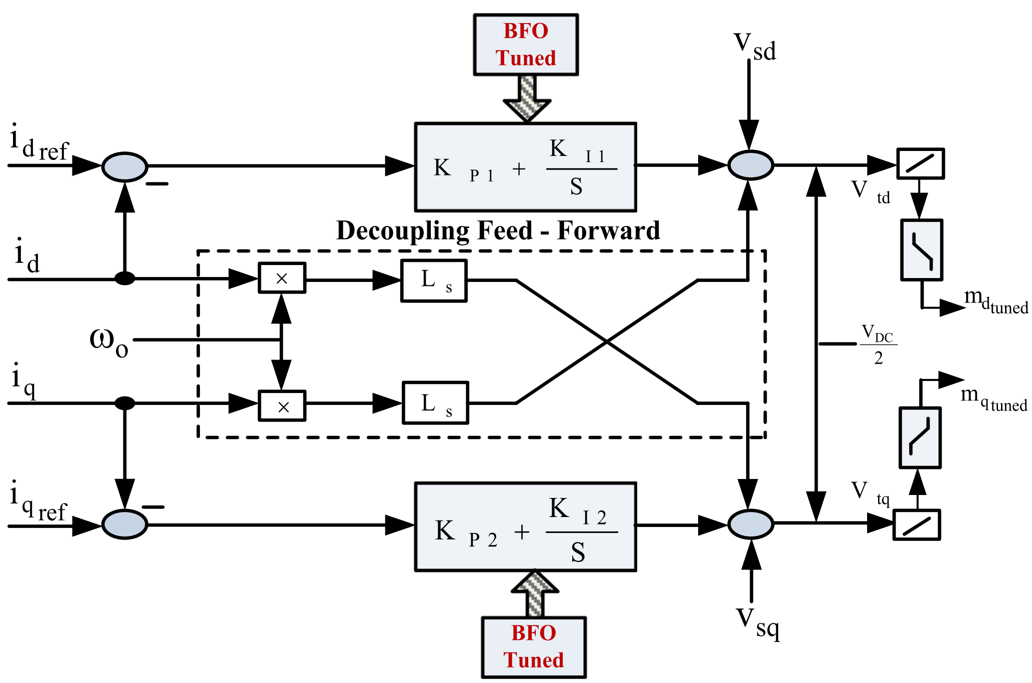

Fig. 5 Current control block

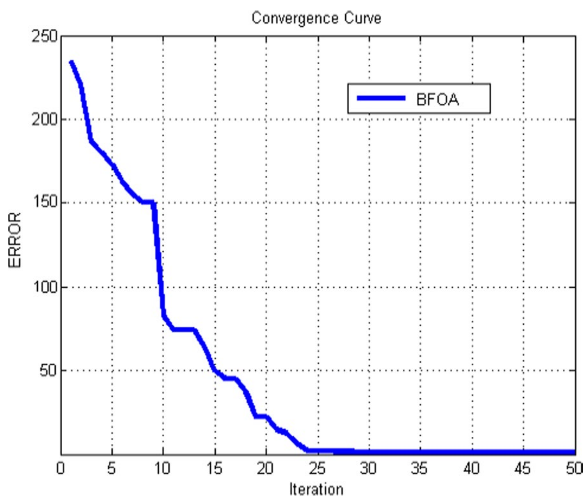

Fig. 6 The controller error with BFO iterations

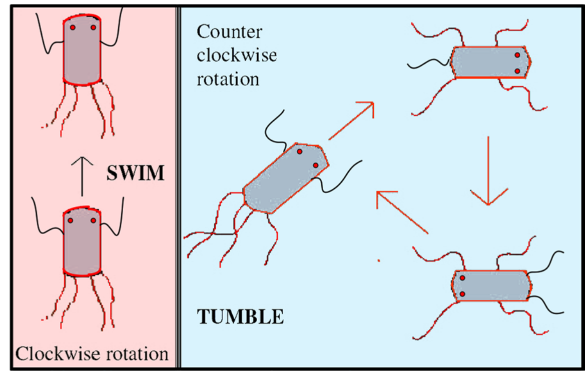

Fig. 7 The bacterial chemotaxis

and the q-axis current I_q matches the desired reference I_{qref} generated by the DC voltage regulator.

The BFO-based metaheuristic-swarm optimizer is deployed to optimally select the PI controller gain to promptly reduce the errors to the least value. Once the d-q components of the line currents I_d and I_q match the desired reference values I_{dref} and I_{qref}, the direct and quadrature errors, i.e. ($I_{dref} - I_d$) and ($I_{qref} - I_q$), approach zero. Figure 6 presents the error against the number of BFO iterations, obtained using Matlab.

The control blocks are identical to those of the controller used in the inverter control in [20] except for tuning the controller parameters with a 'trial and error' approach. In this paper, the MPPT-based DC voltage controller and current PI controller gains are selected with the BFO optimization technique to obtain the desired results.

The lagging VAR injected from the Solar-PV inverter is regulated following the rotor deviations, resulting in a required voltage variation at the coupling bus. The voltage is modulated so that a compensating current is driven in the alternator armature windings. The current components are such that they alleviate the rotor oscillations, including sub-synchronous oscillations due to series compensated lines. In addition, the modulated voltage also stabilizes the PCC voltage as per the system requirements.

4.2 Optimal controller parameter selection using the BFO algorithm

The BFO detailed theory has been discussed in [48, 49].

4.3 Rule-based BFOA heuristics

In the present study, the primitive metaheuristic BFO optimizer is customized and tailored to suit the complexity and problem dimensions of current interest. This reduces the computational time without altering the accuracy. The new BFOA heuristics state:

- The controller gain is made the function of bacterial positions in the problem search space.
- The bacteria continuously change their position with set heuristics. The gain and performance matrices are altered accordingly until they converge to a location that brings a suboptimal/optimal solution with a gain that extracts the desired objective in a particular search space with a fixed dimension and certain bacterial count.
- The primitive BFO optimizer follows conventional chemotaxis with a set run length and hence is not easily adaptable to the new problem dimensions that lead to extra computational burden accompanied by prolonged convergence time.
- Conventional chemotaxis movements of BFO with a fixed step length lead to slow convergence.
- The new heuristics redefine the chemotaxis movements. The modified chemotaxis is now adaptable to problems with arbitrary dimensions and complexity.
- The new chemotaxis with adaptive run-length alters and augments the step size while the observed bacterial movement is in the right direction, and acquires the desired gain and decreases the run-length by the same amount.
- The new chemotaxis with customized heuristics leads to a steeper convergence and reduced computational burden without compromising accuracy.

The BFO algorithm is summarized as follows.

[Step 1] Initialization of BFO parameters p, S, N_c, N_s, N_{re}, N_{ed}, P_{ed}, $C(i)(i=1, 2...S)$, θ^i:

i. p: Search area dimension
ii. S: Bacteria count
iii. N_s: Swim-length
iv. Nc: Chemotaxis steps
v. N_{re}: Reproduction stages
vi. N_{ed}: Elimination-dispersal stages
vii. P_{ed}: Elimination-dispersal chances of the bacteria
viii. The bacterial position P $(j, k, l)=\{\phi^i (j, k, l)$ for $i=1, 2,...,S\}$ is the bacterial location amid S bacteria at the jth chemotaxis, kth reproduction, and lth elimination-dispersal stage
ix. C(i): Run-length which is held constant for the simple design.

The bacterial chemotactic movements including swim and tumble are shown in Fig. 7. The bacterial movements and actual bacterial positions during BFO optimization are portrayed in Fig. 8.

[Step 2] $l=l+1$: Perform Elimination-dispersal;
[Step 3] $k=k+1$: Perform Reproduction;
[Step 4] $j=j+1$: Perform Chemotaxis;

[a] For $i=1, 2...S$, perform chemotaxis for the ith bacterium

[b] Evaluate the cost $J (i, j, k, l)$ at the ith bacterial location $\phi^i (j, k, l)$
*J has been interchangeably used to represent the cost (optimization theory) and chemotactic movement related to the nutrient surface (Biological process).

Let, $J (i, j, k, l)=J (i, j, k, l)+J_{cc} (\theta^i (j, k, l), P(j, k, l))$, where the subscript cc stands for cell-to-cell signalling in the bacterial swarm.

Let $J_{last}=J (i, j, k, l)$
Tumble: Vector initialization $\Delta(i)$, with elements lying in the range $[-1, 1]$. $\Delta(i) \in \Re^p$ with each element $\Delta_m(i), m = 1, 2, \ldots, p$.
Move: Let

$$\theta^i(j+1,k,l) = \theta^i(j,k,l) + C(i)\frac{\Delta(i)}{\sqrt{\Delta^T(i)\Delta(i)}}$$

Step size $C(i)$ coincides with the bacterial tumble direction.

[f] Evaluate, $J (i, j+1, k, l)$.
Let

$$J(i,j+1,k,l) = J(i,j,k,l) + J_{cc}(\theta^i(j+1,k,l), P(j+1,k,l).$$

[g] Swimi) Let $m=0$ (swim-length counter)ii) While, $m<N_s$,

- Let $m=m+1$
- If J $(i, j+1, k, l)<J_{last}$,
- let $J_{last}=J(i, j+1, k, l)$,
- and let $\theta^i(j+1,k,l) = \theta^i(j,k,l) + C(i)\frac{\Delta(i)}{\sqrt{\Delta^T(i)\Delta(i)}}$

Use $\theta^i(j+1,k,l)$ to evaluate new J $(i, j+1, k, l)$.
Else, let $m=N_s$.
[h] Jump to the next bacterial $(i+1)$, if $i \neq S$ (jump to [b] to process the next bacterial).

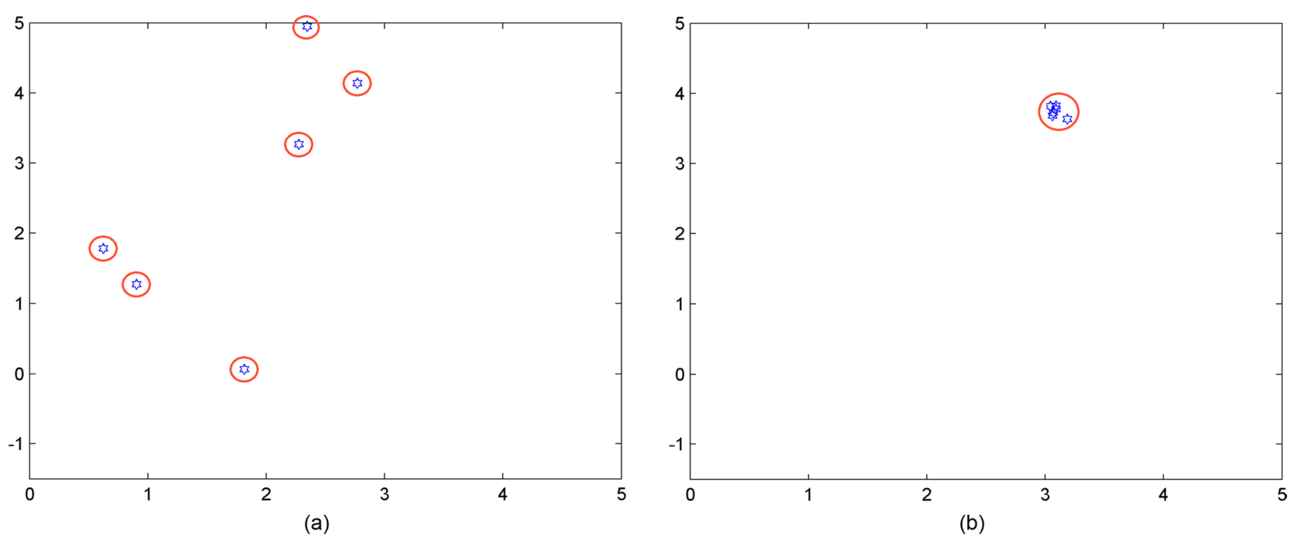

Fig. 8 The bacterial swarm during optimization **a** the initial bacterial position, **b** the final bacterial position on convergence

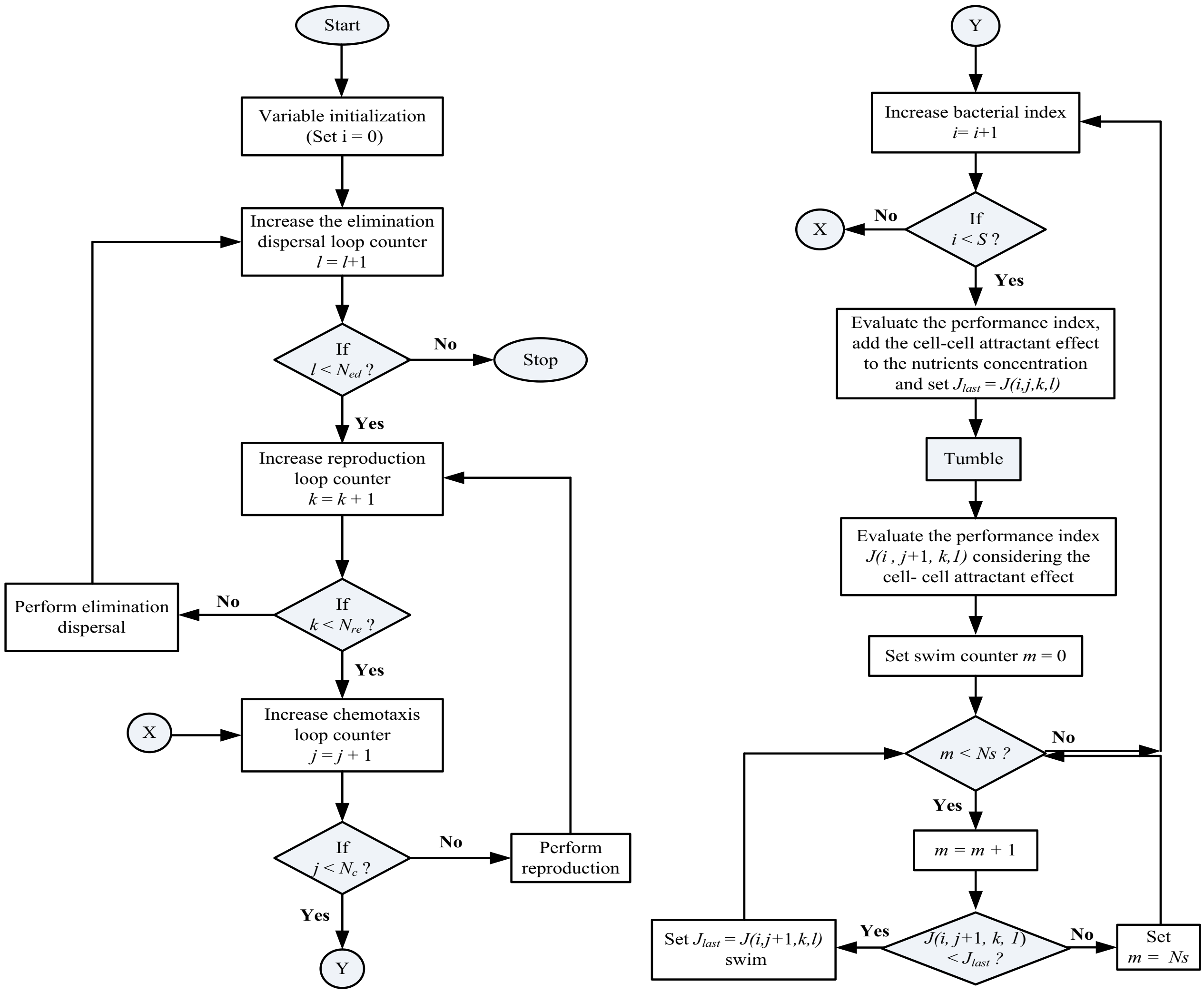

Fig. 9 The BFO algorithm

[Step 5] If $j < N_c$, jump to Step 4, and continue the chemotactic movements.

[Step 6] Reproduction:

[a] For k, l and $i = 1, 2,\ldots\ldots, S$,let

$$J^i_{health} = \sum_{j=1}^{N_c+1} J(i,j,k,l)$$

mathematically presents the ith bacterial health (health measures the bacterial fitness in terms of nutrients availed by the individual bacteria). Arrange the bacterial and chemotactic parameters $C(i)$ in the scaling (increasing) cost J_{health} (high cost means poor health).

[b] The S_r bacterium having utmost J_{health} dies and the rest of the bacteria, having fewer J_{health} (i.e., sound health), grow and split.

[Step 7] If $k < N_{re}$, jump to Step 3. Here, the required reproduction stages have not been reached, hence initiating the next chemotaxis.

[Step 8] Elimination-dispersal: For $i = 1, 2,\ldots., S$ having probability P_{ed}, perform elimination-dispersal for the individual bacteria (this maintains the bacterial count at a fixed value).

This is achieved by dispersing bacteria at an arbitrary location on account of bacterial elimination. If $l < N_{ed}$, jump to Step 2; else end the process.

The BFO flowchart comprising different steps of optimization is shown in Fig. 9. In the present work the BFO parameters are (S = 6; Ns = 2; NC = 10; Nre = 2; Ned = 2; Ped = 0.2; Sr = S/2).

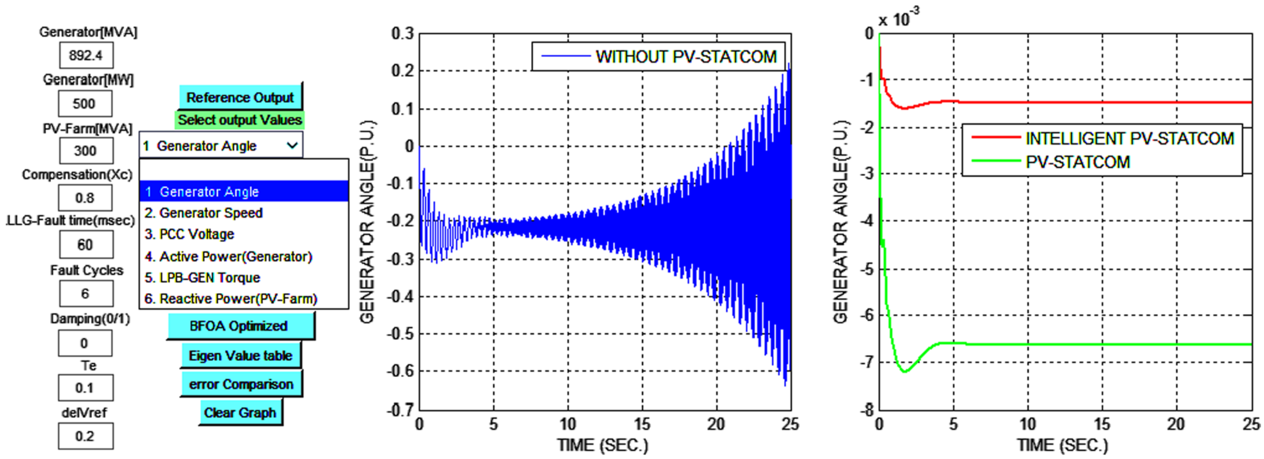

Fig. 10 Generator angle deviation (Δδ)

5 Analytical results

This paper demonstrates the ability of a large-scale solar farm to dampen the oscillations by rapidly exchanging the active and reactive powers at the common bus. Kundur's modified model aggregated with a 300 MVA large-scale PV-farm (containing 300 individual PV-generators) is realized in the Matlab/Simulink domain to test and demonstrate the dynamic behavior of alternator power angle (δ), speed (ω), active power (P), lagging VAR (Q) and the shaft torsions while the system experiences a 3-ϕ, 6-cycle, LLLG fault. The critical clearing time is 60 ms. A series capacitor of appreciable capacitance is connected in the line between buses 8–9 to set an optimal compensation of 80%. Compensating a line at such an optimal level boosts the natural parameters of the line. This leads to an appreciable amount of natural current in the line connected to the armature terminals. Such natural currents cause forced mechanical oscillations to the rotor at a sub-synchronous frequency causing SSR that ultimately leads to damage to interconnecting shaft segments at the rotor. The inertial constants of all the machine elements have been considered zero for the true realization of the worst scenario. Additionally, the system is also perturbed by introducing a variable (20%) stator terminal voltage (ΔV_{ref}) and a varying (10%) counter electromagnetic torque by altering X_d''. This also introduces an additional disturbance exactly analogous to the perturbance caused by a 3-ϕ fault. The overall chaos produced is stabilized using the grid-tied Solar-PV plant working as a Solar-PV inverter. A swarm-based intelligent optimizer BFO optimally controls the MPPT DC voltage controller [20]. The PI parameters of the inverter control system, estimated by the Ziegler-Nichol method for K_p and K_i are 46.45 and 1, whereas the BFO-optimized K_p and K_i are 198.57 and 2.76, respectively. The simulation outcomes for deviations in the generator angle, speed, active power, variations in the common point voltage (ΔV), and the torsional modes for the cases, viz. without/with the Solar-PV inverter, and with the suggested BFO-based Solar-PV inverter demonstrate the capabilities of the recommended controlling topology in mitigating and stabilizing the multiple disturbances simultaneously. A user interface is designed in Matlab to realize the outcomes more precisely and to be user-friendly. The GUI input corresponding to the disturbances introduced is the numeric values in decimals. For example, the user interface input for an 80% compensated line is 0.8, and inputs for 10% and 20% variations in electromagnetic torque and reference voltage are 0.1 and 0.2, respectively. A damping value of zero means the system's inertial constants are neglected, and input 1 means the inertial constants are considered.

5.1 Transient stability with zero natural dampings

The system experiences a 3-ϕ, 6-cycle**,** LLLG fault at 3 s for 60 ms. Although the alternators integrated into the system have their natural inertia, the inertia of the alternators is not considered in the proposed work so that the effect of the natural damping may be obviated. The line is compensated optimally at 80% with zero inertial constants.

A 10% variation in the counter-electric torque accompanied by a 20% variation in the set armature voltage are additional disturbances to simulate worse circumstances. The oscillatory movements for the machine's different modes of current interest are portrayed in Figs. 10, 11, 12, 13, 14 and 15.

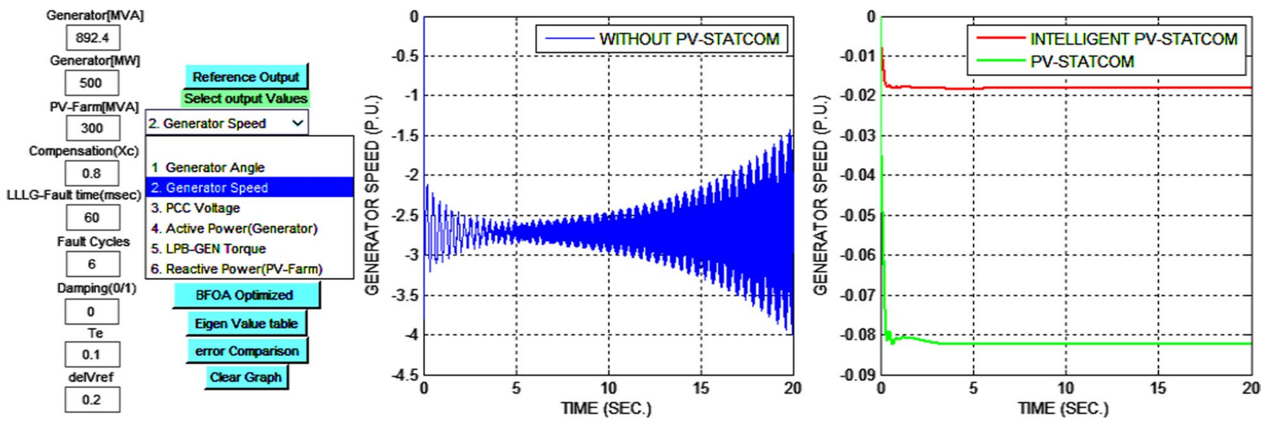

Fig. 11 Rotor speed deviation (Δω)

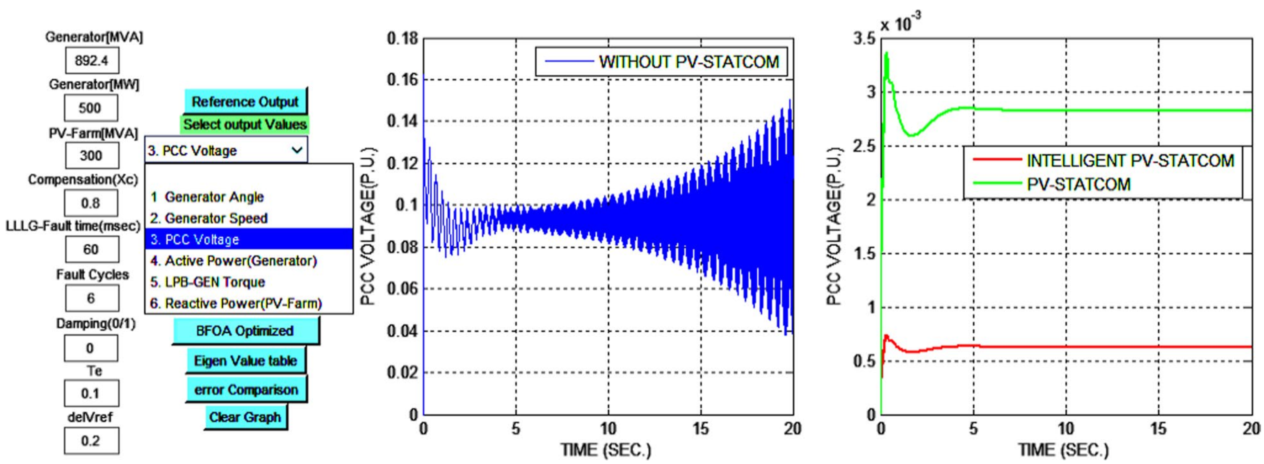

Fig. 12 Coupling voltage deviation (ΔV)

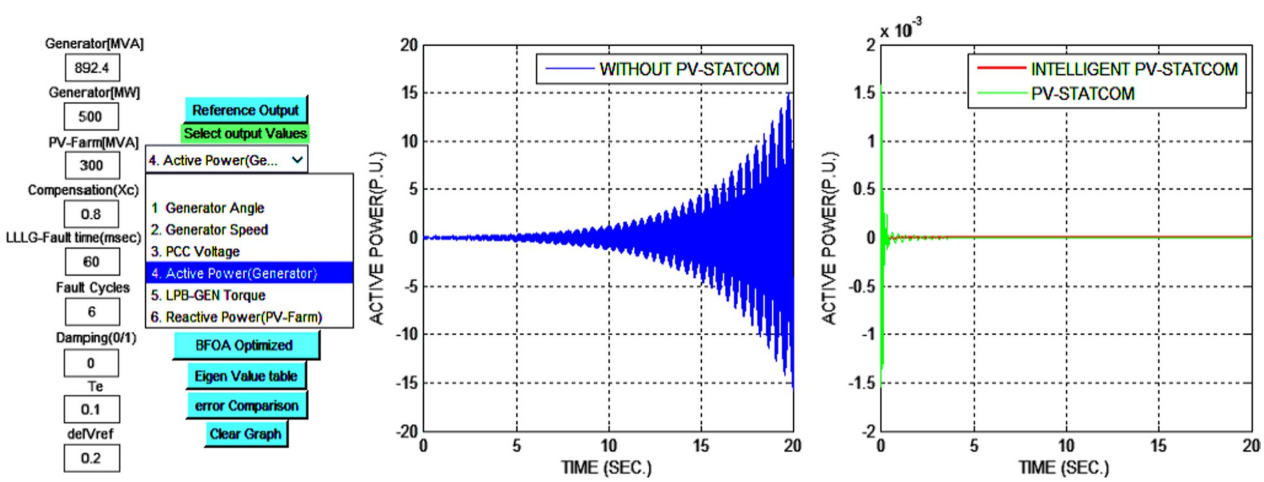

Fig. 13 Active power deviations (ΔP)

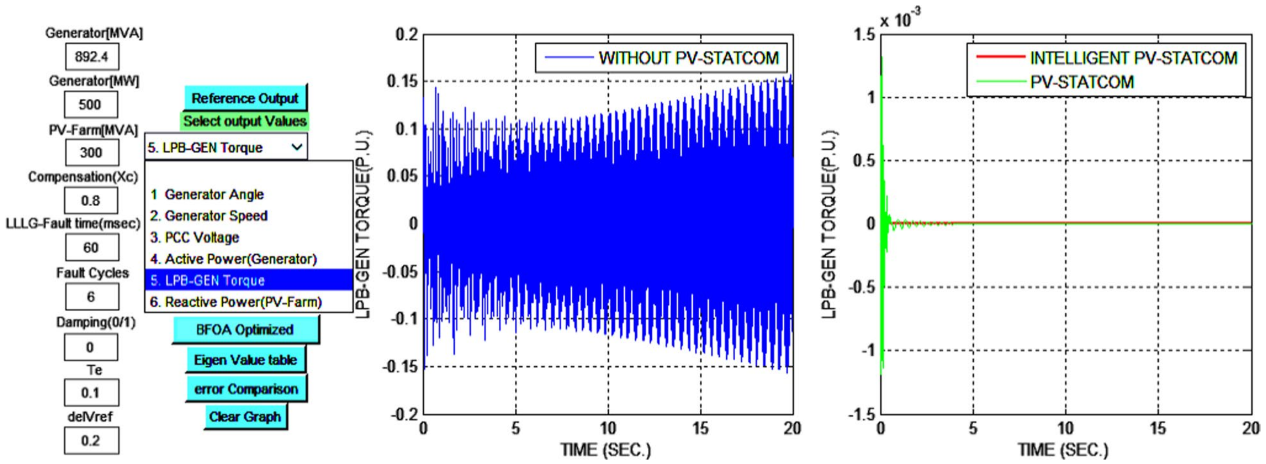

Fig. 14 Torsional deviations ($\Delta\tau_{Lp_B-Gen}$)

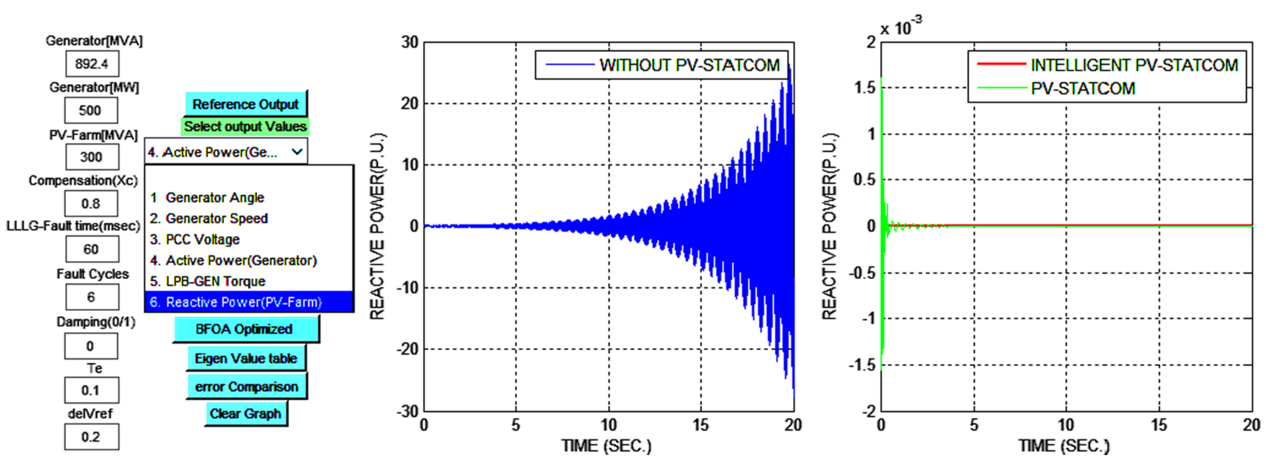

Fig. 15 Reactive power deviations (ΔQ)

Table 2 Transient eigenvalues

Torsion mode-eigenvalue/damping ratios			
Torsion-mode	**Without solar-PV inverter**	**With solar-PV inverter**	**With BFO-based solar-PV inverter**
5th Mode	(1.246e−04 ± 296.61i)/− **4.20080e−07**	(− 0.78961 ± 296.59i)/**2.66228e−03**	(− 1.12589 ± 296.58i)/**3.79621e−03**
4th Mode	(− 0.3629 ± 200.04i)/**1.814134e−03**	(− 3.5223 ± 200.02i)/**1.76070e−02**	(− 4.2456 ± 200.01i)/**2.12221e−02**
3rd Mode	(− 0.2369 ± 160.59i)/**1.47518e−03**	(− 5.3258 ± 160.76i)/**3.31107e−02**	(− 6.4752 ± 160.74i)/**4.02510e−02**
2nd Mode	(− 0.1285 ± 122.11i)/**1.05232e−03**	(− 4.2153 ± 121.17i)/**3.47672e−02**	(− 5.3698 ± 121.16i)/**4.42764e−02**
1st Mode	(− 0.5468 ± 97.26i)/**5.62195e−03**	(− 3.4552 ± 97.21i)/**3.55212e−02**	(− 4.1592 ± 97.20i)/**4.27510e−02**
0th Mode	(− 0.4586 ± 5.29i)/**8.63679e−02**	(− 3.2356 ± 5.21i)/**5.27575e−01**	(− 4.14785 ± 5.20i)/**6.23580e−01**
Other mode	Stable	stable	stable
Electric mode-eigenvalue/damping ratios			
Electrical-Mode	(− 0.0221 ± 191.2i)/**1.15585e−04**	(− 2.1615 ± 190.6i)/**1.13397e−02**	(− 4.2629 ± 190.4i)/**2.23835e−02**

Bold indicates Damping Ratios

Table 3 Time domain specifications (transient state)

Generators rotor dynamics			
Generator angle (δ)	**Without solar-PV inverter**	**With solar-PV inverter**	**With BFO-based solar-PV inverter**
Settling time (s)	Undefined	3.79	1.17
%Overshoot	Undefined	**14.226%**	**8.168%**

Bold indicates Percentage(%) Overshoot

A thorough time domain analysis of the different modes has been presented in the eigenvalues [56] in Table 2. The eigenvalue and damping ratio for the 5th mode seem unstable, and the electrical mode is marginally stable while the PV-plant is generating power at its full capacity so the Solar-PV inverter is not available for power oscillation damping. A considerable improvement in the eigenvalues is observed for the modes once the Solar-PV inverter is available for oscillation damping. The eigenvalues continue to improve while the BFO is controlling the Solar-PV inverter. The eigenvalues of the 0–4th modes are observed to be negative and stable even in the absence of the Solar-PV inverter. Nevertheless, the eigenvalues become more negative and are improved with the Solar-PV inverter. Further, the eigenvalues continue to improve and become more negative while the BFO is operating with the Solar-PV inverter. As the alternators of the multi-machine system are identical and coherent, and placed in an identical environment, the dynamic behavior of one of the machines is sufficient to represent the conditions of the other machines in the areas of interest.

As presented in Figs. 10, 11, 12, 13, 14 and 15, a monotonous increase in the oscillations of the rotor angle and speed (Δδ, Δω), machine active-reactive powers (ΔP-ΔQ), common point voltage (ΔV), and torsional modes have been observed while the PV-plant is in active power generation and the Solar-PV inverter is not available for mitigating the oscillations. The oscillations are settled once the Solar-PV inverter starts working to dampen the

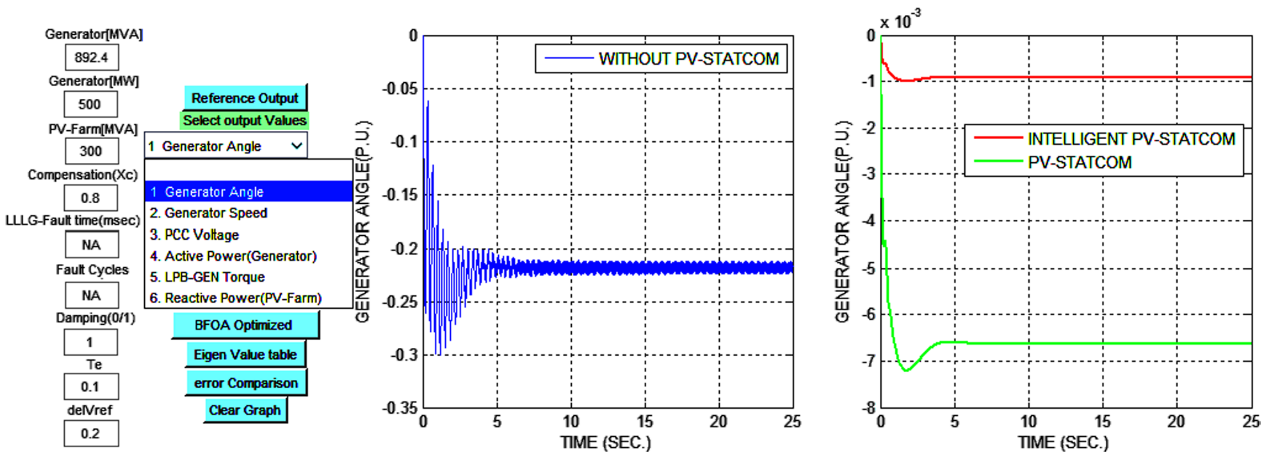

Fig. 16 Generator angle deviation (Δδ)

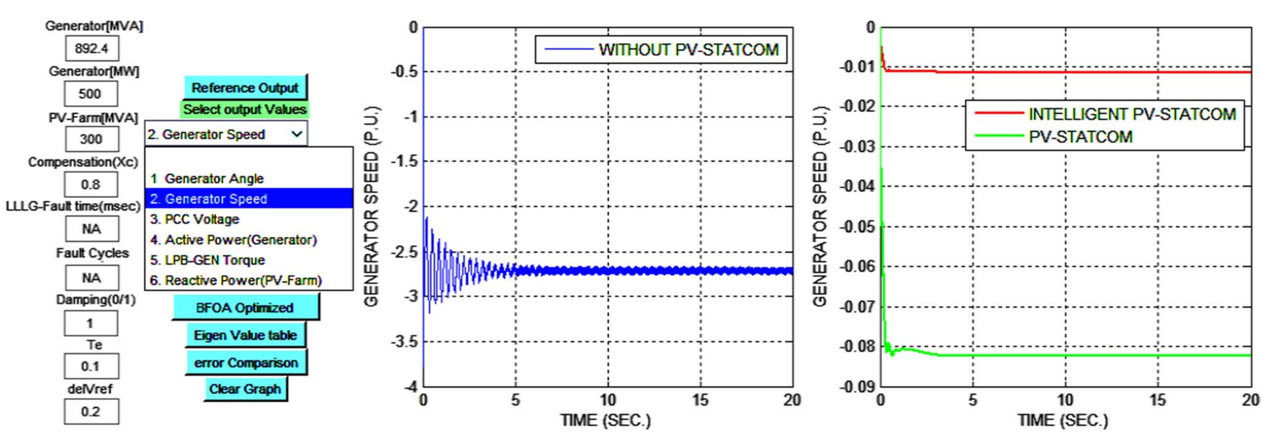

Fig. 17 Rotor speed deviation (Δω)

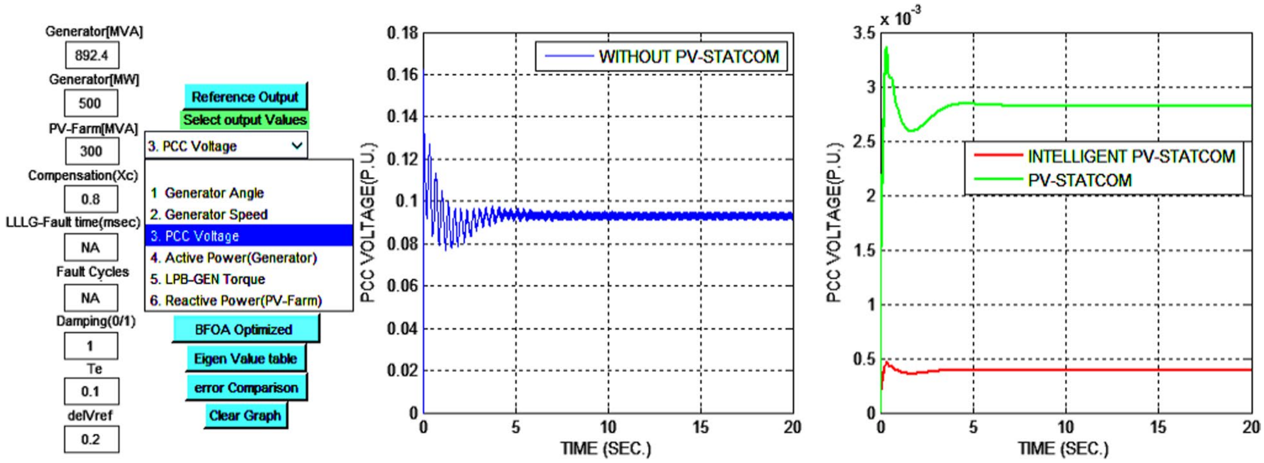

Fig. 18 Coupling voltage deviation (ΔV)

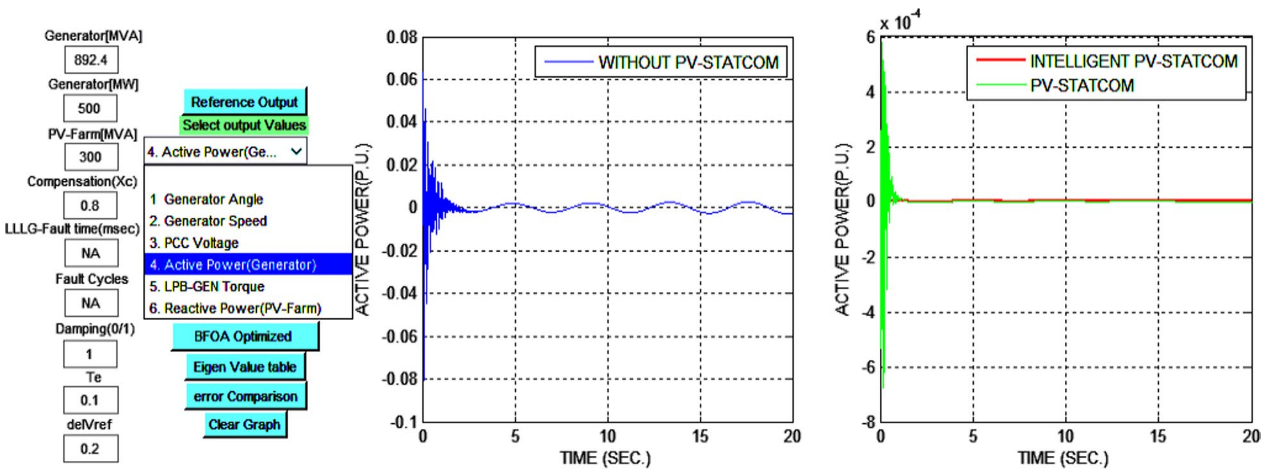

Fig. 19 Active power deviations (ΔP)

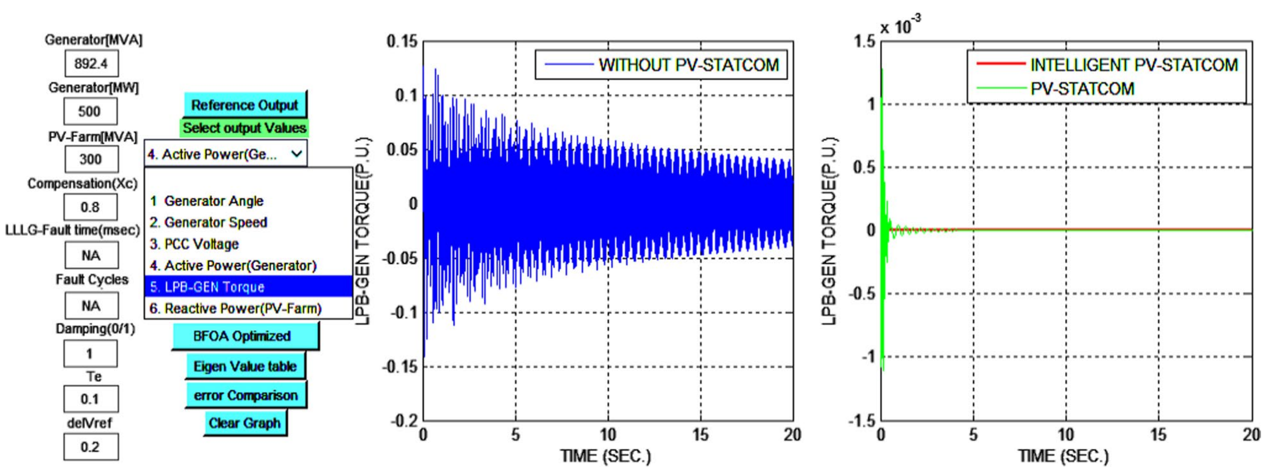

Fig. 20 Torsional deviations ($\Delta\tau_{Lp_B-Gen}$)

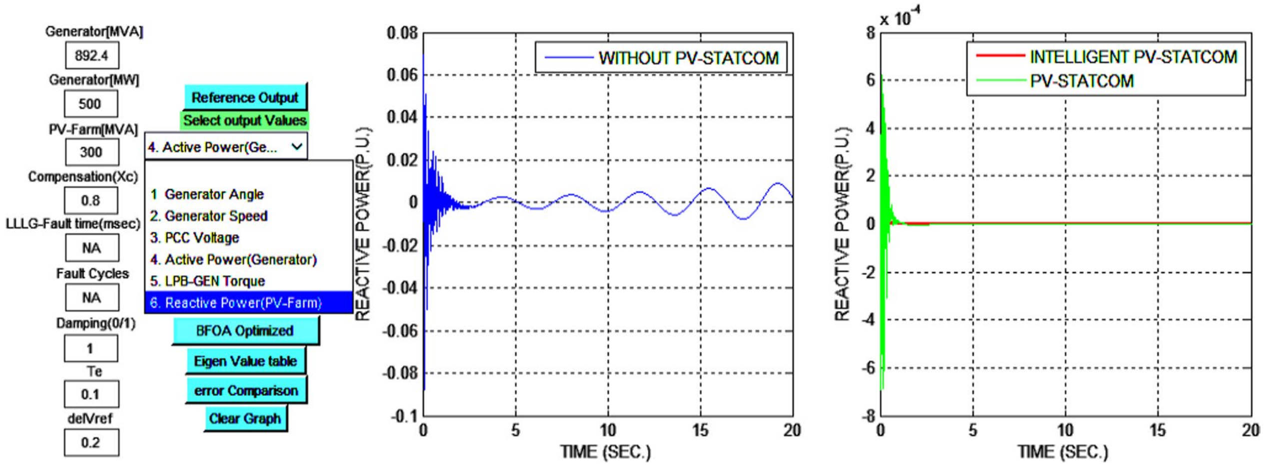

Fig. 21 Reactive power deviations (ΔQ)

Table 4 Steady-state eigenvalues

Eigenvalue/damping ratios			
Torsion-mode	**Without solar-PV inverter**	**With solar-PV inverter**	**With BFO-based solar-PV inverter**
5th Mode	(− 0.4633 ± 295.19i)/**1.60205e−03**	(− 2.7521 ± 295.18i)/**9.32305e−03**	(− 3.32561 ± 295.17i)/**1.1266e−02**
4th Mode	(− 1.1478 ± 200.68i)/**5.71946e−03**	(− 3.1478 ± 200.66i)/**1.56853e−02**	(− 4.2164 ± 200.65i)/**2.1009e−02**
3rd Mode	(− 2.3695 ± 159.51i)/**1.48532e−02**	(− 4.3578 ± 159.50i)/**2.73114e−02**	(− 5.3785 ± 159.51i)/**3.3699e−02**
2nd Mode	(− 3.1452 ± 124.39i)/**2.52769e−02**	(− 5.7569 ± 124.38i)/**4.62352e−02**	(− 6.1982 ± 124.37i)/**4.9775e−02**
1st Mode	(− 1.1596 ± 97.26i)/**1.19218e−02**	(− 4.5987 ± 97.24i)/**4.72394e−02**	(− 5.4462 ± 97.21i)/**5.5937e−02**
0th Mode	(− 1.3215 ± 5.10i)/**2.50832e−01**	(− 4.1634 ± 5.09i)/**6.33133e−01**	(− 5.25641 ± 5.08i)/**7.1906e−01**
Other mode	Stable	Stable	Stable
Electric mode-eigenvalue/damping ratios			
Electrical-mode	(− 0.0756 ± 191.69i)/**3.94386e−04**	(− 3.2685 ± 190.23i)/**1.71792e−02**	(− 5.9634 ± 190.21i)/**3.13362e−02**

Bold indicates Damping Ratios

oscillations. The improvement continues and the system gains considerable stability while the BFO optimizer starts controlling the Solar-PV inverter.

Table 3 portrays the rotor oscillatory parameters in terms of percentage overshoot and settling time while the inertial constants of the machines are neglected. The results reflect that both the parameters of the machines are unspecified without the Solar-PV inverter because of the 3-ϕ fault, 10% variation in the electromechanical torque, and 20% variation in the reference voltage. Nevertheless, by applying PV-STATCOM, the deviations are controlled and later significantly suppressed by deploying the suggested BFO-based Solar-PV inverter.

5.2 Steady-state stability analysis with natural damping

Variations in the rotor angle and speed (Δδ, Δω), machine active-reactive powers (ΔP-ΔQ), common point voltage(ΔV), and torsional modes are shown in Figs. 16, 17, 18, 19, 20 and 21, while the steady-state eigenvalues are presented in Table 4.

Table 5 Time domain specifications (Steady state)

Generator rotor dynamics			
Generator angle (δ)	**Without solar-PV inverter**	**With solar-PV inverter**	**With BFO-based solar-PV inverter**
Settling time (s)	5.2	3.02	1.11
%Overshoot	44.325%	7.665%	3.881%

The eigenvalue table reveals the stability of all the modes in the absence of the Solar-PV inverter, while the eigenvalues became more negative wit the involvement of the inverter. The negative amplitudes of the eigenvalues continue to grow when the BFO tunes the Solar-PV inverter control parameters.

The results presented in Figs. 16, 17, 18, 19, 20 and 21 demonstrate that the deviations in power angle, rotor speed, active and reactive powers, common point voltage, and shaft torsions, are suppressed and alleviated with the Solar-PV inverter. Once the BFO starts acting over the Solar-PV inverter controller, the oscillations are further suppressed and the system becomes more stabilized. The settling time and overshoot percentage are presented in Table 5, illustrating that both parameters are minimized using the Solar-PV inverter and attained the least values by deploying the suggested BFO optimizer on the basic PV-STATCOM controller. The less negative electric mode eigenvalues and smaller initial damping ratios reveal poor damping of the system, i.e., the system is marginally stable and may lose synchronism in the absence of the Solar-PV inverter. Figures 10, 11, 12, 13, 14 and 15 in the transient analysis and Figs. 16, 17, 18, 19, 20 and 21 in the steady-state analysis also portray and confirm the poor and marginally stable electrical and torsional modes which may be unstable at any moment when the Solar-PV inverter is fully absent for the oscillation damping while generating power. The electrical mode eigenvalues become considerably negative and the electrical mode damping is substantially improved once the Solar-PV inverter starts operating as PV-STATCOM to alleviate and suppress the oscillations. The eigenvalues become most negative and the oscillations are most settled when the proposed BFO optimizer starts functioning over the Solar-PV inverter.

6 Conclusion

The outcomes explicitly demonstrate the potential of the BFO algorithm when deployed on the basic PV-STATCOM control in suppressing power oscillations in a two-area power system. The proposed model is developed in Matlab to examine the deviations in the machine rotor angle and speed ($\Delta\delta$, $\Delta\omega$), active and reactive powers (ΔP-ΔQ), common point voltage (ΔV), and shaft torsion. The examination is performed for different cases, e.g., in the absence of the Solar-PV inverter, in the presence of the Solar-PV inverter, and when the suggested BFO-optimizer started controlling the Solar-PV inverter. Natural damping of the test system is permitted for steady state analysis, while it was discarded and set to zero for the transient studies to exhibit worse conditions. This enables an exact and adequate examination of the suggested controller's potential in both states. The eigenvalues for the machine dynamics in both states for various cases manifest the merits of the proposed BFO-based Solar-PV inverter in suppressing the oscillations of the multi-machine system.

Acknowledgements
None.

Authors' contributions
SS: Original draft preparation, Conceptualization, Methodology, Software, Data curation, Formal analysis. SS: Supervision, Reviewing, and Editing. SKG: Reviewing, and Editing. RK: Conceptualization, Methodology, Original draft preparation, Software, Supervision, Reviewing, and Editing, Validation. All authors read and approved the final manuscript.

Funding
No funding has been received for this work.

Availability of data and materials
Data sharing not applicable to this article as no datasets were generated or analysed during the current study.

Declarations

Competing interests
The authors declare that they have no known competing financial interestsor personal relationships that could have appeared to influence the work reported in this paper.

Received: 11 October 2022 Accepted: 15 March 2023
Published online: 06 April 2023

References

1. Mohammadpour, H. A., & Santi, E. (2015). SSR damping controller design and optimal placement in rotor-side and grid-side converters of series-compensated DFIG-based wind farm. *IEEE Transactions on Sustainable Energy, 6*(2), 388–399.
2. Liu, H., Xie, X., Zhang, C., Li, Y., Liu, H., & Hu, Y. (2017). Quantitative SSR analysis of series-compensated DFIG-based wind farms using aggregated RLC circuit model. *IEEE Transactions on Power Systems, 32*(1), 474–483.
3. Kumar, R., Khetrapal, P., Badoni, M., & Diwania, S. (2022). Evaluating the relative operational performance of wind power plants in Indian electricity generation sector using two-stage model. *Energy and Environment, 33*(7), 1441–1464. https://doi.org/10.1177/0958305X211043531
4. Kumar, R., Diwania, S., Khetrapal, P., Singh, S., & Badoni, M. (2021). Multimachine stability enhancement with hybrid PSO-BFOA based PV-STATCOM. *Sustainable Computing Informatics and Systems*. https://doi.org/10.1016/j.suscom.2021.100615
5. Kumar, R., Diwania, S., Khetrapal, P., & Singh, S. (2022). Performance assessment of the two metaheuristic techniques and their hybrid for power system stability enhancement with PV-STATCOM. *Neural Computing and Applications, 34*, 3723–3744. https://doi.org/10.1007/s00521-021-06637-9
6. International Energy Agency PV Power System Task1 Report, Trends in photovoltaic applications—survey report of selected IEA countries between 1992–2010; 2011.
7. PV Resources, Large scale photovoltaic power plants ranking 1–50, 2016. http://www.pvresources.com/en/pvpowerplants/top50pv.php#notes
8. Sunpower, Solar Projects, Solar Star Projects. (2016). http://us.sunpower.com/utility-scale-solar-power-lants/solarenergy-projects/solar-star-projects/
9. First Solar Projects. (2016). http://www.firstsolar.com/About-Us/Projects.aspx
10. First Solar Projects, Agua Caliente Solar Project. (2016). http://www.firstsolar.com/About-Us/Projects/Agua-Caliente-Solar-Project
11. R.Shah, N.Mithulananthan, Y. Lee Kwang, "Large-scale PV plant with a robust controller considering power oscillation damping," *IEEE Trans. Energy Convers.*, vol. 28, no. 1, pp. 106–116, 2013.
12. Shah, R., Mithulananthan, N., & Bansal, R. C. (2013). Oscillatory stability analysis with high penetrations of large-scale photovoltaic generation. *Energy Conversion and Management, 65*, 420–429.
13. Shah, R., Mithulananthan, N., Sode-Yome, A., & Lee, K. Y. (2010). Impact of large-scale PV penetration on power system oscillatory stability. In *IEEE-PES general meeting*, Minneapolis, USA, July 25–28.

14. Shah, R., Mithulananthan, N., & Bansal, R. C. (2012). Damping performance analysis of battery energy storage, ultracapacitor, and shunt capacitor with large-scale PV plants. *Applied Energy Special Issue Smart Grid, 96*, 235–244.
15. Varma, R. K., Khadkikar, V., & Seethapathy, R. (2009). Nighttime application of PV solar farm as STATCOM to regulate grid voltage. *IEEE Transactions on Energy Conversion, 24*(4), 983–985.
16. Varma, R. K., Khadkikar, V., & Rahman, S. A. (2010). Utilization of distributed generator inverters as STATCOM. PCT Patent application PCT/CA2010/001419 filed on, September 15, 2010.
17. Varma, R. K., Rahman, S. A., & Vanderheide, T. (2015). Novel control of PV solar farm as STATCOM(PV-STATCOM) for enhancing grid power transmission limits during night and day. *IEEE Transactions on Power Delivery, 30*(2), 755–763.
18. Shah, R., Mithulananthan, N., Bansal, R., & Ramachandaramurthy, V. (2015). A review of key power system stability challenges for large-scale PV integration. *Renewable and Sustainable Energy Reviews, 41*, 1423–1436.
19. Varma, R. K. (2014). Multivariable modulator controller for power generation facility. PCT Application (PCT/CA2014/051174) filed on December 6, 2014.
20. Varma, R. K., & Salehi, R. (2017). SSR mitigation with a new control of PV solar farm as STATCOM (PV-STATCOM). *IEEE Transactions on Sustainable Energy, 8*(4), 1473–1483.
21. Kundur, P., Balu, N. J., & Lauby, M. G. (1994). *Power system stability and control* (Vol. 7). McGraw-Hill.
22. Walker, D. N., Bowler, C. E. J., Jackson, R. L., & Hodges, D. A. (1975). Results of subsynchronous resonance test at Mohave. *IEEE Transactions on Power Apparatus and Systems, PAS-94*(5), 1878–1889.
23. Anderson, P. M., Agrawal, B. L., & Van Ness, J. E. (1990). *Subsynchronous resonance in power systems*. IEEE Press.
24. Padiyar, K. R. (1999). *Analysis of subsynchronous resonance in power systems*. Kluwer.
25. Khayyatzadeh, M., & Kazemzadeh, R. (2017). Sub-synchronous resonance damping using high penetration PV plant. *Mechanical Systems and Signal Processing, 84*, 431–444.
26. Singh, B., Saha, R., Chandra, A., & Al-Haddad, K. (2008). Static synchronous compensators (STATCOM): A review. *IET Power Electronics, 2*(4), 297–324.
27. Wei, S., Zhou, Y., & Huang, Y. (2017). Synchronous motor-generator pair to enhance small signal and transient stability of power system with high penetration of renewable energy. *IEEE Access, 5*, 11505–11512.
28. Varma, R. K., & Maleki, H. (2019). PV solar system control as STATCOM (PV-STATCOM) for power oscillation damping. *IEEE Transactions on Sustainable Energy, 10*(4), 1793–1803.
29. Varma, R. K., & Siavashi, E. M. (2019). Enhancement of solar farm connectivity with smart PV inverter PV-STATCOM. *IEEE Transactions on Sustainable Energy, 10*(3), 1161–1171.
30. Abdulrahman, I., Belkacemi, R., & Radman, G. (2019). Power oscillations damping using wide-area-based solar plant considering adaptive time-delay compensation. *Energy System*. https://doi.org/10.1007/s12667-019-00350-2
31. Li, M., Xiong, L., Chai, H., Xiu, L., & Hao, J. (2020). Mechanism of PV generation system damping electromechanical oscillations. *IEEE Access, 8*, 135853–135865.
32. Silva-Saravia, H., Pulgar-Painemal, H., Tolbert, L. M., Schoenwald, D. A., & Ju, W. (2021). Enabling utility-scale solar PV plants for electromechanical oscillation damping. *IEEE Transactions on Sustainable Energy, 12*(1), 138–147.
33. Chaudhary, P., & Rizwan, M. (2021). QNBP NN-based I cos φ algorithm for PV systems integrated with LV/MV grid. *Soft Computing, 25*, 2599–2614.
34. Rehman, H. U., Yan, X., Abdelbaky, M. A., Jan, M. U., & Iqbal, S. (2021). An advanced virtual synchronous generator control technique for frequency regulation of grid-connected PV system. *Electrical Power and Energy Systems, 125*, 106440. https://doi.org/10.1016/j.ijepes.2020.106440
35. Remon, D., Cantarellas, A. M., Mauricio, J. M., & Rodriguez, P. (2017). Power system stability analysis under increasing penetration of photovoltaic power plants with synchronous power controllers. *IET Renewable Power Generation, 11*(6), 733–741.
36. Kawabe, K., Ota, Y., Yokoyama, A., & Tanaka, K. (2017). Novel Dynamic voltage support capability of photovoltaic systems for improvement of short-term voltage stability in power systems. *IEEE Transactions on Power Systems., 32*(3), 1796–1804.
37. Howlader, A. M., Sadoyama, S., Roose, L. R., & Chen, Y. (2020). Active power control to mitigate voltage and frequency deviations for the smart grid using smart PV inverters. *Applied Energy, 258*, 114000. https://doi.org/10.1016/j.apenergy.2019.114000
38. Varma, R. K., & Akbari, M. (2018). A novel reactive power based frequency control by PV-STATCOMs during day and night. In *2018 IEEE power & energy society general meeting (PESGM)*. Portland, USA. https://doi.org/10.1109/PESGM.2018.8586014.
39. Varma, R. K., & Akbari, M. (2020). Simultaneous fast frequency control and power oscillation damping by utilizing PV solar system as PV-STATCOM. *IEEE Transactions on Sustainable Energy, 11*(1), 415–425.
40. Varma, R. K., & Mohan, S. (2020). Mitigation of fault induced delayed voltage recovery (FIDVR) by PV-STATCOM. *IEEE Transactions on Power Systems., 35*(6), 4251–4262.
41. Kumar, R., Singh, R., & Ashfaq, H. (2020). Stability enhancement of multimachine power systems using Ant colony optimization-based static Synchronous Compensator. *Computers and Electrical Engineering*. https://doi.org/10.1016/j.compeleceng.2020.106589
42. Yao, J., Wang, X., Li, J., Liu, R., & Zhang, H. (2019). Sub-synchronous resonance damping control for series-compensated DFIG-based wind farm with improved particle swarm optimization algorithm. *IEEE Transactions on Energy Conversion, 34*(2), 849–859.
43. Kumar, R., Diwania, S., Singh, R., Ashfaq, H., Khetrapal, P., & Singh, S. (2022). An intelligent hybrid wind-PV farm as a static compensator for overall stability and control of multimachine power system. *ISA Transactions, 123*, 286–302. https://doi.org/10.1016/j.isatra.2021.05.014
44. Kumar, R., Singh, R., Ashfaq, H., Singh, S., & Badoni, M. (2021). Power system stability enhancement by damping and control of Sub-synchronous torsional oscillations using Whale optimization algorithm based Type-2 wind turbines. *ISA Transactionss, 108*, 240–256.
45. Kumar, R., Singh, R., & Ashfaq, H. (2020). Stability enhancement of induction generator-based series compensated wind power plants by alleviating subsynchronous torsional oscillations using BFOA-optimal controller tuned STATCOM. *Wind Energy, 23*, 1846–1867.
46. Abo-Elyousr, F. K., & Abdelaziz, A. Y. (2020). A novel modified robust load frequency control for mass-less inertia photovoltaics penetrations via hybrid PSO-WOA approach. *Electric Power Components and Systems*. https://doi.org/10.1080/15325008.2020.1731867
47. Devarapalli, R., Bhattacharyya, B., & Sinha, N. K. (2020). An intelligent EGWO-SCA-CS algorithm for PSS parameter tuning under system uncertainties. *International Journal of Intelligent Systems*. https://doi.org/10.1002/int.22263
48. Abdul-Ghaffar, H. I., Ebrahim, E. A., & Azzam, M. (2013). Design of PID controller for power system stabilization using hybrid particle swarm-bacteria foraging optimization. *WSEAS Transactions on Power Systems, 1*(8), 2224–2350.
49. Das, S., Biswas, A., Dasgupta, S., & Abraham, A. (2009). Bacterial foraging optimization algorithm: theoretical foundations, analysis, and applications. *Foundations of Computational Intelligence, 3*, 23–55.
50. IEEE Committee Report. (1977). First benchmark model for computer simulation of subsynchronous resonance. *IEEE Transactions on Power Apparatus and Systems, 96*(5), 1565–1572.
51. Rahman, S. A., Varma, R. K., & Vanderheide, T. (2014). Generalized model of a photovoltaic panel. *IET Renewable Power Generation, 8*(3), 217–229.
52. Mao, M., Lichuang, C., Zhang, Q., Guo, K., Zhou, L., & Huang, H. (2020). Classification and summarization of solar photovoltaic MPPT techniques: A review based on traditional and intelligent control strategies. *Energy Reports, 6*, 1312–1327.
53. Yazdani, A., & Iravani, R. (2010). *Voltage-sourced converters in power systems: modeling, control, and applications*. Wiley.
54. Dahono, P. A., Sato, Y., & Kataoka, T. (1996). Analysis and minimization of ripple components of input current and voltage of PWM inverters. *IEEE Transactions on Industry Applications, 32*(4), 945–950.
55. Devarapalli, R., Bhattacharyya, B., Sinha, N. K., et al. (2021). Amended GWO approach based multi-machine power system stability enhancement. *ISA Transactions, 109*, 152–174.
56. Singh, S. K., Singh, R., Ashfaq, H., & Kumar, R. (2022). Virtual inertia emulation of inverter interfaced distributed generation (IIDG) for dynamic frequency stability & damping enhancement through BFOA tuned optimal controller. *Arabian Journal for Science and Engineering, 47*, 3293–3310. https://doi.org/10.1007/s13369-021-06121-5